

Observation of an anomalous heat current in GdPtBi

Clemens Schindler,¹ Stanislaw Galeski,¹ Satya N. Guin,¹ Walter Schnelle,¹ Nitesh Kumar,¹ Chenguang Fu,¹ Horst Borrmann,¹ Chandra Shekhar,¹ Yang Zhang,¹ Yan Sun,¹ Claudia Felser,¹ Tobias Meng,² Adolfo G. Grushin,³ and Johannes Gooth^{1,*}

¹Max Planck Institute for Chemical Physics of Solids, D-01187 Dresden, Germany

²Institute of Theoretical Physics, Technische Universität Dresden, D-01062 Dresden, Germany

³Univ. Grenoble Alpes, CNRS, Grenoble INP, Institut Néel, 38000, Grenoble, France

(Dated: April 17, 2022)

In condensed matter Weyl systems, it is predicted^{1–6} that the generation of a heat current by the mixed axial-gravitational anomaly leads to a negative magnetothermal resistivity (MTR), locked to the parallel alignment of the applied temperature gradient ∇T and magnetic field \mathbf{H} . Here, we show magnetothermal transport experiments on the semimetal GdPtBi, which has previously been reported to host Weyl fermions^{7–9}. For collinear temperature gradients and magnetic fields ($\nabla T \parallel \mathbf{H}$), we observe a negative MTR, which diminishes at high magnetic fields, when ∇T is aligned perpendicular to \mathbf{H} . This observation is consistent with the generation of an anomalous heat current. At low fields, however, we also observe a negative MTR for $\nabla T \perp \mathbf{H}$, suggesting a more complex origin of the magnetothermal transport properties of GdPtBi.

Weyl fermions are realized as low-energy quasiparticles in certain semimetals with topologically protected crossing points of two electronic bands^{10–12}. They occur in pairs of independent nodes, separated in momentum space with opposite chirality - a quantum number defining the 'handedness' of a quasiparticle's spin relative to its momentum. Classically, the particle number of each chirality is separately conserved. However, at the quantum level electromagnetic fields and space-time curvature can violate the conservation of the particle number at individual nodes due to quantum fluctuations. This phenomenon is known as the chiral anomaly^{13,14}. The electromagnetic contribution to the chiral anomaly is well understood¹⁴. Physically, it can be interpreted as simultaneous production of particles of one chirality and anti-particles of the opposite chirality in parallel electric and magnetic fields $\mathbf{E} \parallel \mathbf{H}$. With the particle/anti-particle production rate being proportional to $a_c \mathbf{E} \cdot \mathbf{H}$, where a_c is a universal universal constant. In the context of Weyl semimetals, the chiral anomaly is expected to induce a steady out-of-equilibrium flow of quasiparticles between the left- and right-handed nodes, leading to an enhancement of magnetoconductivity^{6,7,15–23}.

Much less studied is the gravitational contribution to the chiral anomaly, i.e. the mixed axial-gravitational anomaly^{14,24}. In this case, the production rate of particles and anti-particles of opposite chirality is proportional to $a_g R R^*$, where the Riemann tensor R , and its dual R^* , describe the curvature of space-time and a_g is a characteristic constant - the gravitational anomaly coefficient (see SI for details). Intuitively, the mixed axial-gravitational anomaly should be irrelevant to condensed matter experiments in flat space-time as the Riemann tensor vanishes in the absence of space-time curvature ($R = 0$). However, a recent multidisciplinary theoretical effort^{3,6,25–29} has found that transport coefficients of chiral fermions can fingerprint a_g even for $R = 0$. It was shown that a_g enters the equations for heat transport

in Weyl fermion systems even in the case of flat space-time, leading to a negative magnetothermal resistivity (MTR) for magnetic fields aligned with the thermal gradient (see SI). Despite the apparent similarity with the chiral anomaly in electrical transport, the experimental detection of the mixed axial-gravitational anomaly in thermal transport has yet remained elusive. The main experimental challenge being the extremely low density of electronic states of Weyl systems, which renders thermal transport heavily dominated by phononic conduction.

Here, we present magnetothermal transport experiments in the prototypical Weyl fermion material GdPtBi. Employing steady-state thermal resistance measurements with stabilization times up to an hour per data point, we achieved a $0.05 \text{ WK}^{-1} \text{ m}^{-1}$ resolution. This enabled us to extract the electronic contribution to the thermal resistivity from a two orders of magnitude higher phononic background. In collinear magnetic fields, our heat transport data is in good agreement with the scenario of an anomaly-induced negative longitudinal MTR. Applying the magnetic field perpendicular to the temperature gradient, however, our experiments reveal a more complicated magneto-thermal transport behaviour, which cannot be solely explained by Weyl physics.

The GdPtBi samples used in our study were grown in Bi self-flux³⁰. The high quality of the samples was established using X-ray diffraction (for details see SI) and confirmed by the presence of pronounced quantum oscillations (Fig. 1d). For transport measurements, the sample was aligned along the [100]-axis and cut into a regular bar of $2.7 \times 0.6 \times 0.4 \text{ mm}^3$. All measurements have been performed in a Quantum Design PPMS system equipped with a 9 T magnet. In all experiments, the electrical and thermal currents, \mathbf{J} and \mathbf{J}_h , were applied along the [100]-axis with the magnetic field \mathbf{H} rotated in the [010]-plane. Electrical resistivity measurements were performed in a 4-point configuration using standard lock-in technique with a frequency of 93 Hz and excita-

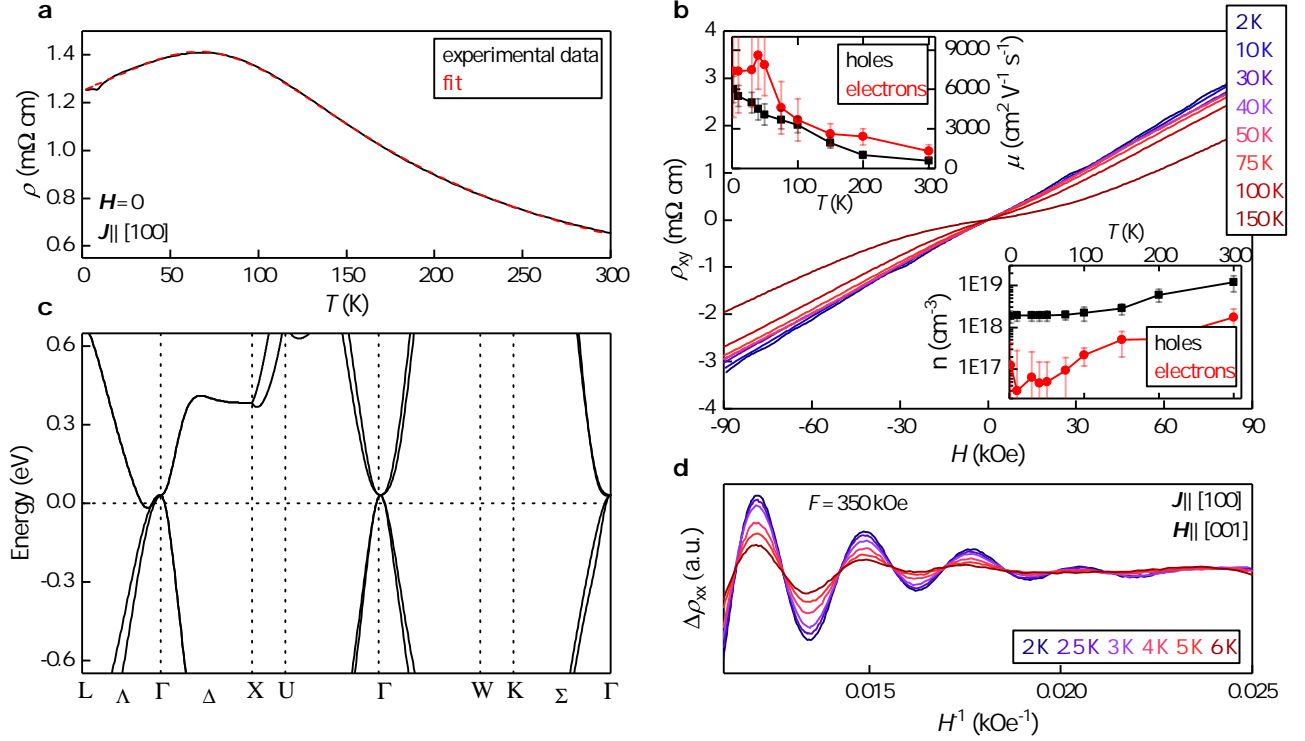


FIG. 1. Electronic characterization of our GdPtBi sample. a) Zero-field resistivity $\rho(T)$. The dashed red line shows a fit with a thermally excited two-carrier model³⁷. b) Hall resistivity $\rho_{xy}(H)$ for $\mathbf{H} \perp \mathbf{J}$ for different temperatures. The insets show the T -evolution of the carrier mobilities μ and densities n extracted from a two-carrier fit of ρ_{xy} . c) Band structure of GdPtBi from density functional theory. d) Shubnikov-de Haas oscillations at low temperatures show a single frequency $F = 350$ kOe corresponding to the hole pocket along Γ -X.

tion currents in the range of 1 – 10 mA. Hall measurements were performed in a 5-point configuration, balancing the Hall resistance to less than 10 nΩ at $\mathbf{H} = 0$. To achieve good thermal coupling to the sample for thermal resistance measurements, we have fabricated four thermal contacts using 0.6×0.25 mm² gold-plated Cu-bars for the heater and the heat sink; and 0.1 mm Pt-wire for the thermometers. In order to avoid thermal smearing, the heater power was set such that the temperature gradient ΔT does not exceed 3% of the sample temperature T . In addition, in both electrical and thermal measurements contacts were wrapped around the sample and attached with silver paint to assure current homogeneity at an expense of a geometrical error due to the contact size (not more than 10%). The magneto-electrical resistivity (MR) ρ_{xx} and MTR w_{xx} have been symmetrized with respect to $\mathbf{H} = 0$, and the Hall resistivity ρ_{xy} antisymmetrized, respectively, to eliminate small misalignment effects.

In a first set of electrical transport experiments, we establish that our GdPtBi sample shows the same characteristics as those reported by refs. 7 and 8. The electrical resistivity $\rho(T)$ at $H = 0$ exhibits a semimetallic behaviour (Fig. 1a), where the thermal activation of charge carriers causes a decrease in $\rho(T)$ above 75 K. The sharp cusp at 9 K has been reported to occur due to

the formation of a small superzone gap of 1 meV at the antiferromagnetic ordering of Gd's 4*f*-moments^{31–36}.

Above 10 K, $\rho(T)$ can be described with a thermally excited two-carrier model³⁷ (for details see SI). Consistently, the Hall resistivity $\rho_{xy}(H)$ exhibits an increasingly non-linear slope upon rising T (see Fig. 1b). Using a two-carrier Drude model, we have extracted the carrier mobilities and densities (Fig. 1b inset) from the Hall data (see SI for details). The hole density is in the order of $10^{18} - 10^{19}$ cm⁻³ and is about an order of magnitude larger than the electron density, with the electron/hole ratio decreasing towards lower temperatures. According to these findings and our band structure calculations (see SI for details), our sample can be well described as having one dominant hole pocket close to the band crossing points. Through the analysis of the Shubnikov-de Haas (SdH) oscillations we have estimated the Fermi level of our sample to lie at (29 ± 2) meV from the nearest band touching point (see SI for details), in agreement with previous reports on GdPtBi^{7,36}. The corresponding effective mass $m_{\text{eff}} = 0.29 m_e$ and Fermi wavevector $k_F = 0.033 \text{ \AA}^{-1}$ (estimated assuming a circular Fermi surface), match the hole band along $\Gamma - X$ (e.g. [100]) calculated from density functional theory (DFT) (see Fig. 1c).

The zero-field temperature dependence of the thermal

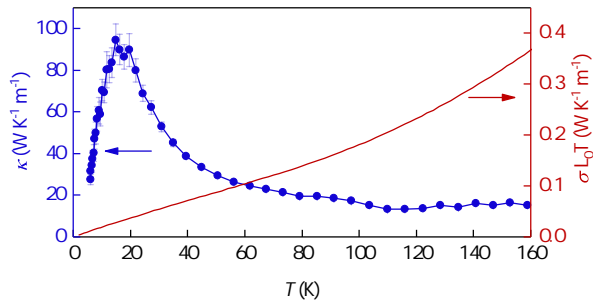


FIG. 2. Left axis: Zero-field thermal conductivity $\kappa(T)$. Right axis: Estimated electronic contribution κ_{el} from the Wiedemann-Franz law.

conductivity $\kappa(T)$ is displayed in Fig. 2 (left axis). As expected for semimetals, the overall T -dependence of the thermal transport in GdPtBi can be explained by phonon conduction: upon warming from 2 K, $\kappa(T)$ increases with T^3 due to the increasing lattice heat capacity. Near 15 K, $\kappa(T)$ reaches a maximum of around $95 \text{ W K}^{-1} \text{ m}^{-1}$ and then starts to decrease exponentially due to the onset of phonon Umklapp scattering. At higher T , the exponential drop is replaced by a slower $1/T$ power law dependence. The electronic contribution κ_{el} is estimated by the Wiedemann-Franz law $\kappa_{\text{el}} \approx L_0 T / \rho$, with the Lorenz number $L_0 = 2.44 \cdot 10^{-8} \text{ W} \Omega \text{ K}^{-2}$, and is illustrated in Fig. 2 (right axis). Above the antiferromagnetic transition temperature, changes in κ upon applying a magnetic field are expected to originate from the electronic contribution. Since GdPtBi has not shown signs of short-range correlations in the paramagnetic phase⁸, and the quadrupole moment of Gd is zero, magnetoelastic effects altering the phonon density should be negligible³⁸. This allows for the experimental access of κ_{el} via magnetothermal transport measurements, assuming a constant phononic background. However, since the ratio $\kappa_{\text{el}}/\kappa_{\text{ph}}$ strongly decreases upon lowering T , a lower limit of $\kappa_{\text{el}}/\kappa_{\text{ph}} \approx 1/500$ is set at 30 K by the sensitivity of our thermometers.

Application of a magnetic field leads to a large negative contribution to both the MR $\Delta\rho_{xx}(H)/\rho_{xx}(0)$ and the MTR $\Delta w_{xx}(H)/w_{xx}(0)$ for longitudinal \mathbf{H} and $T \leq 100 \text{ K}$ (see Figs. 3c,d), varying from an inverse quadratic field-dependence at higher T towards a bell-shape at low T . For low fields, the negative longitudinal contribution follows an inverse quadratic function, in good accordance with the Boltzmann equation for the chiral magnetic effect for both electrical and thermal transport (for details see SI). The field range, where the low-field Boltzmann model fits, is similar for the longitudinal magneto-electrical and magneto-thermal conductivities for comparable T (see SI). Importantly, also the maximum T , up to which the anomaly-related contributions are observed, is similar for both electrical and thermal transport.

The transverse MR and MTR at high T are

positive and follow a quadratic dependence at low fields (Figs. 3a,b). This behaviour is typical for semimetals^{39–41} and can partly be explained by two-carrier compensation (see refs. 39 and 42 and also SI). At low temperatures and low fields, a region of negative MR is also observed in the transverse configuration, which has previously been ascribed to the formation of Weyl nodes^{7,43}. However, the SdH oscillations in our sample do not display a distinguishable sign of a band splitting or a decreasing Fermi surface in the measured field range, which is at odds with such a Weyl node creation process. Interestingly, the transverse MTR also displays an intriguing substructure below 50 K for magnetic fields up to 60 kOe, emerging congruently with the oscillatory features in the transverse MR (see Fig. 3a). We note that in comparison to the electrical resistance, the negative transverse MTR at low fields is of the same size as the negative MTR in longitudinal fields, which seems at odds with the first order anomaly-related magnetotransport predictions. Notably, the two-carrier Lorentz contribution for the MTR scales with T (see ref. 42 and SI), which is reflected in a weakening of the positive contribution upon lowering the temperature (Fig. 3b). Therefore, the prominence of the negative substructure in the transverse MTR as compared to the MR might be due to the vanishing of the Lorentz contribution in thermal magnetoresistance at low temperatures.

Consistent with a recent work⁴⁴, our DFT calculations revealed the possible existence of triple point crossings along the $\Gamma - \text{L}$ -line, situated around 10 meV below the Fermi level. The occurrence of triple point fermions was recently predicted to occur in a number of Heusler compounds⁴⁵ and might have an effect on the magnetotransport when close to the Fermi level. In fact, it is predicted that the existence of triple fermions could lead to quantum anomalies akin to those of Weyl fermions⁴⁶. However, we found similar band structure features in the non-magnetic YPtBi (see SI), without any signatures of quantum anomalies being reported⁸. This suggests that a careful investigation of the interplay of band structure and effect of localized f -electron magnetic moments is required to fully account for the emergence of the negative magnetoresistance in both thermal and electrical transport.

Our experimental results reveal a negative magnetothermal resistivity in collinear temperature gradients and magnetic fields in GdPtBi, a material widely believed to host Weyl fermions. This seems consistent with the reported anomalous electrical and thermoelectrical responses. The thermal transport data is in good agreement with the semiclassical models of the mixed axial-gravitational anomaly in the low magnetic field-regime. However the transverse responses to both thermal and electrical currents exhibit features that cannot be accounted for in the simple chiral anomaly picture and require further studies, exploring the interplay of localized moments and non-trivial band structure features.

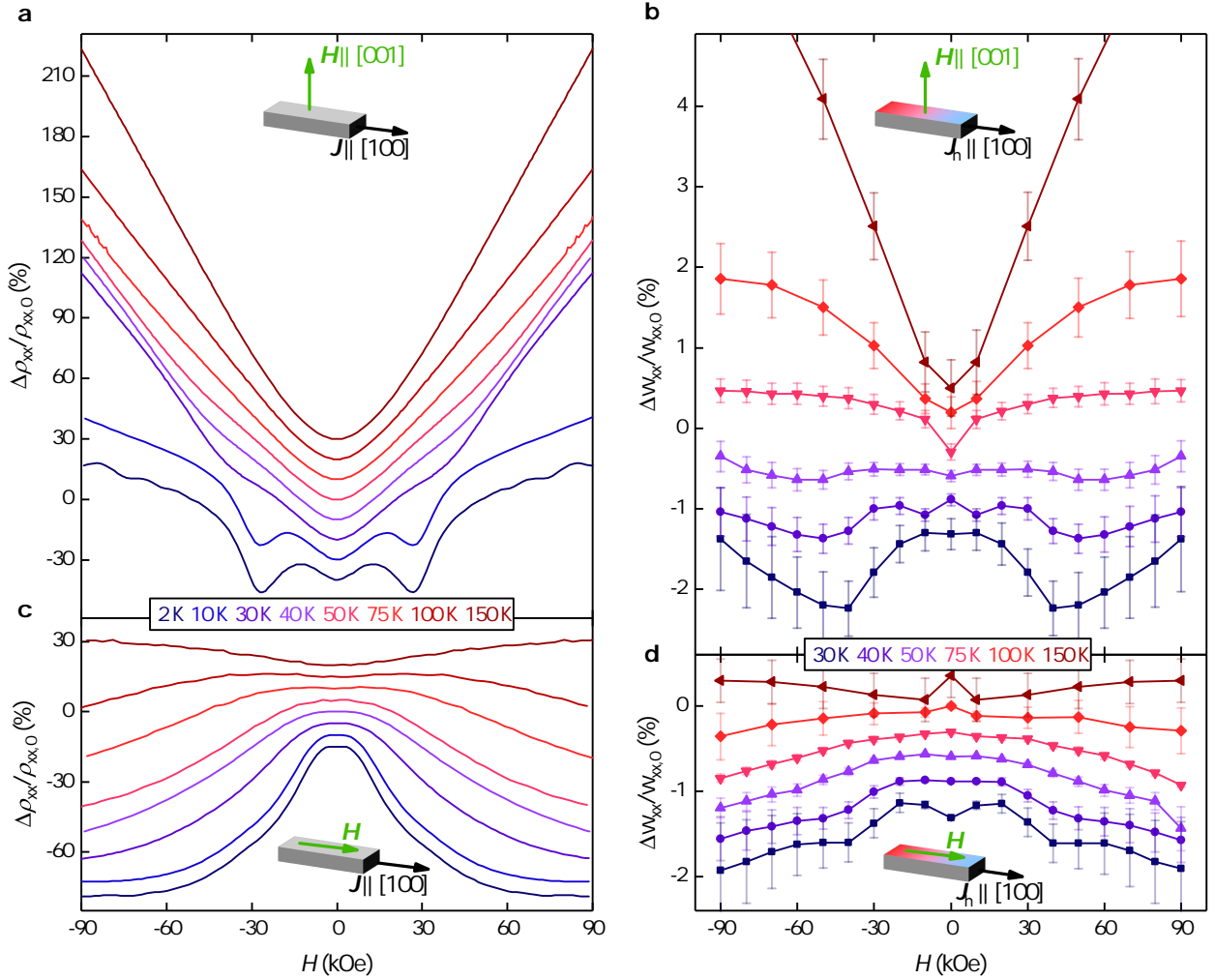


FIG. 3. Anisotropic magnetotransport of GdPtBi. (a,c) Magnetoresistance $\Delta\rho_{xx}(H)/\rho_{xx}(0)$ for (a) transverse and (c) longitudinal H -configuration. (b,d) Magnetothermal resistance $\Delta w_{xx}(H)/w_{xx}(0)$ of GdPtBi for (b) transverse and (d) longitudinal H -configuration. The curves are shifted by constant offsets for better visibility.

ACKNOWLEDGMENTS

A. G. G. thanks J. Cano, B. Bradlyn and R. Ilan for engaging in clarifying discussions. A. G. G. acknowledges financial support from the Marie Curie programme under EC Grant agreement No. 653846. T. M. acknowledges funding by the Deutsche Forschungsgemeinschaft through the Emmy Noether Programme ME 4844/1-1

and through SFB 1143. Cl. S. thanks R. Koban for providing technical support and C. Geibel for engaging in clarifying discussions. This work was financially supported by the ERC Advanced Grant No. 291472 Idea Heusler and ERC Advanced Grant No. 742068 TOP-MAT. Cl. S. acknowledges financial support by the International Max Planck Research School for Chemistry and Physics of Quantum Materials (IMPRS-CPQM).

* johannes.gooth@cpfs.mpg.de

¹ Burkov, A. A. Chiral anomaly and transport in Weyl metals. *J. Phys. Cond. Mat.* **27**, 113201 (2015).

² Kharzeev, D. E. The chiral magnetic effect and anomaly-induced transport. *Prog. Part. Nucl. Phys.* **75**, 133–151 (2014).

³ Lucas, A., Davison, R. A. & Sachdev, S. Hydrodynamic theory of thermoelectric transport and negative magne-

toresistance in Weyl semimetals. *Proc. Natl. Acad. Sci. USA* **113**, 9463–9468 (2016).

⁴ Lundgren, R., Laurell, P. & Fiete, G. A. Thermoelectric properties of Weyl and Dirac semimetals. *Phys. Rev. B* **90**, 165115 (2014).

⁵ Sharma, G., Goswami, P. & Tewari, S. Nernst and magnetothermal conductivity in a lattice model of Weyl fermions. *Phys. Rev. B* **93**, 035116 (2016).

- ⁶ Gooth, J. *et al.* Experimental signatures of the mixed axial-gravitational anomaly in the Weyl semimetal NbP. *Nature* **547**, 324–327 (2017).
- ⁷ Hirschberger, M. *et al.* The chiral anomaly and thermopower of Weyl fermions in the half-Heusler GdPtBi. *Nat. Mater.* **15**, 1161–1165 (2016).
- ⁸ Shekhar, C. *et al.* Anomalous Hall effect in Weyl semimetal half-Heusler compounds RPtBi (R = Gd and Nd). *Proc. Natl. Acad. Sci. USA* **115**, 9140–9144 (2018).
- ⁹ Kumar, N., Guin, S. N., Felser, C. & Shekhar, C. Planar Hall effect in the Weyl semimetal GdPtBi. *Phys. Rev. B* **98**, 041103 (2018).
- ¹⁰ Armitage, N. P., Mele, E. J. & Vishwanath, A. Weyl and Dirac semimetals in three-dimensional solids. *Rev. Mod. Phys.* **90**, 015001 (2018).
- ¹¹ Xu, S.-Y. *et al.* Discovery of a Weyl Fermion semimetal and topological Fermi arcs. *Science* **349**, 613–617 (2015).
- ¹² Lu, L. *et al.* Experimental observation of Weyl points. *Science* **361**, 622–624 (2015).
- ¹³ Nielsen, H. B. & Ninomiya, M. The Adler-Bell-Jackiw anomaly and Weyl fermions in a crystal. *Phys. Lett. B* **130**, 389–396 (1983).
- ¹⁴ Bertlmann, R. A. *Anomalies in Quantum Field Theory* (Oxford Univ. Press, 2000).
- ¹⁵ Son, D. T. & Spivak, B. Z. Chiral anomaly and classical negative magnetoresistance of Weyl metals. *Phys. Rev. B* **88**, 104412 (2013).
- ¹⁶ Kim, H.-J. *et al.* Dirac versus Weyl Fermions in topological insulators: Adler-Bell-Jackiw anomaly in transport phenomena. *Phys. Rev. Lett.* **111**, 246603 (2013).
- ¹⁷ Huang, X. *et al.* Observation of the Chiral-Anomaly-Induced Negative Magnetoresistance in 3D Weyl Semimetal TaAs. *Phys. Rev. X* **5**, 031023 (2015).
- ¹⁸ Xiong, J. *et al.* Evidence for the chiral anomaly in the Dirac semimetal Na₃Bi. *Science* **350**, 413–416 (2015).
- ¹⁹ Li, Q. *et al.* Chiral magnetic effect in ZrTe₅. *Nat. Phys.* **12**, 550–554 (2016).
- ²⁰ Li, C.-Z. *et al.* Giant negative magnetoresistance induced by the chiral anomaly in individual Cd₃As₂ nanowires. *Nat. Comm.* **6**, 10137 (2015).
- ²¹ Wang, H. *et al.* Chiral anomaly and ultrahigh mobility in crystalline HfTe₅. *Phys. Rev. B* **93**, 165127 (2016).
- ²² Lv, Y. Y. *et al.* Experimental observation of anisotropic Adler-Bell-Jackiw anomaly in type-II Weyl semimetal WTe_{1.98} crystals at the quasiclassical regime. *Phys. Rev. Lett.* **118**, 096603 (2017).
- ²³ Zhang, C. L. *et al.* Signatures of the Adler-Bell-Jackiw chiral anomaly in a Weyl fermion semimetal. *Nat. Comm.* **7**, 10735 (2016).
- ²⁴ Landsteiner, K. Notes on Anomaly Induced Transport. *Acta Phys. Polon. B* **47**, 2617 (2016).
- ²⁵ Jensen, K., Loganayagam, R. & Yarom, A. Thermodynamics, gravitational anomalies and cones. *J. High Energy Phys.* **2**, 88 (2013).
- ²⁶ Golkar, S. & Sethi, S. Global anomalies and effective field theory. *J. High Energy Phys.* **5**, 105 (2016).
- ²⁷ Chowdhury, S. D. & David, J. R. Global gravitational anomalies and transport. *J. High Energy Phys.* **12**, 116 (2016).
- ²⁸ Landsteiner, K., Megías, E., Melgar, L. & Pena-Benitez, F. Holographic gravitational anomaly and chiral vortical effect. *J. High Energy Phys.* **9**, 121 (2011).
- ²⁹ Landsteiner, K., Megías, E. & Pena-Benitez, F. Gravitational Anomaly and Transport Phenomena. *Phys. Rev. Lett.* **107**, 021601 (2011).
- ³⁰ Canfield, P. C. & Fisk, Z. Growth of single crystals from metallic fluxes. *Philos. Mag. B* **65**, 1117–1123 (1992).
- ³¹ Suzuki, T. *et al.* Large anomalous Hall effect in a half-Heusler antiferromagnet. *Nat. Phys.* **12**, 1119–1123 (2016).
- ³² Müller, R. A. *et al.* Magnetic structure of GdBiPt: A candidate antiferromagnetic topological insulator. *Phys. Rev. B* **90**, 041109(R) (2014).
- ³³ Kreyssig, A. *et al.* Magnetic order in GdBiPt studied by x-ray resonant magnetic scattering. *Phys. Rev. B* **84**, 220408 (2011).
- ³⁴ Canfield, P. C. *et al.* Magnetism and heavy fermion-like behavior in the RBiPt series. *J. Appl. Phys.* **70**, 5800–5802 (1991).
- ³⁵ Mun, E., Bud'ko, S. L. & Canfield, P. C. Robust tunability of magnetoresistance in half-Heusler RPtBi (R= Gd, Dy, Tm, and Lu) compounds. *Phys. Rev. B* **93**, 115134 (2016).
- ³⁶ Hirschberger, M. *Quasiparticle Excitations with Berry Curvature in Insulating Magnets and Weyl Semimetals* (Princeton Univ., 2017).
- ³⁷ Berger, St. *et al.* Crystal structure and thermoelectric properties of novel skutterudites Ep_yNi₄Sb_{12-x}Sn_x with Ep = Sn, Eu and Yb. *Proc. 21st International Conference on Thermoelectrics IEEE*, 48 (2002).
- ³⁸ Engdahl, G. *Handbook of Giant Magnetostrictive Materials*. In: Electromagnetism (Elsevier Science, 1999).
- ³⁹ Leahy, I. A. *et al.* Nonsaturating large magnetoresistance in semimetals. *Proc. Natl. Acad. Sci. USA* **115**, 10570–10575 (2018).
- ⁴⁰ Ali, M. N. *et al.* Large, non-saturating magnetoresistance in WTe₂. *Nature* **514**, 205–208 (2014).
- ⁴¹ Shekhar, C. *et al.* Extremely large magnetoresistance and ultrahigh mobility in the topological Weyl semimetal candidate NbP. *Nat. Phys.* **11**, 645–649 (2015).
- ⁴² Honig, J. & Harman, T. Galvano-thermomagnetic effects in multi-band models. *Adv. Energy Conv.* **3**, 529–536 (1963).
- ⁴³ Cano, J. *et al.* Chiral anomaly factory: Creating Weyl fermions with a magnetic field. *Phys. Rev. B* **95**, 161306 (2017).
- ⁴⁴ Hütt, F. *et al.* Linear-in-Frequency Optical Conductivity in GdPtBi due to Transitions near the Triple Points. *Phys. Rev. Lett.* **121**, 176601 (2018).
- ⁴⁵ Barik, R. K., Shinde, R., & Singh, A. K. Multiple triple-point fermions in Heusler compounds. *J. Phys. Condens. Matter* **30**, 375702 (2018).
- ⁴⁶ Lepori, L., Burrello, M., & Guadagnini, E. Axial anomaly in multi-Weyl and triple-point semimetals. *J. High Energy Phys.* **6**, 110 (2018).

Supplementary Information: Observation of an anomalous heat current in GdPtBi

Clemens Schindler *et al.*

I. Crystallographic analysis

The crystal structure of GdPtBi consists of convoluted face centered cubic lattices of the three constituent elements Gd, Pt and Bi; and is part of the cubic space group $F\bar{4}3m$ with the lattice constant $a = 6.68 \text{ \AA}$. The single-crystalline nature of our sample was confirmed by using single crystal X-ray diffraction technique. The diffraction images for the three main crystal axes are shown in Fig. S1, where the characteristic fcc-reflexes are clearly observable for all three directions. The rings in the images most likely stem from powder contaminations on the surface due to the polishing process.

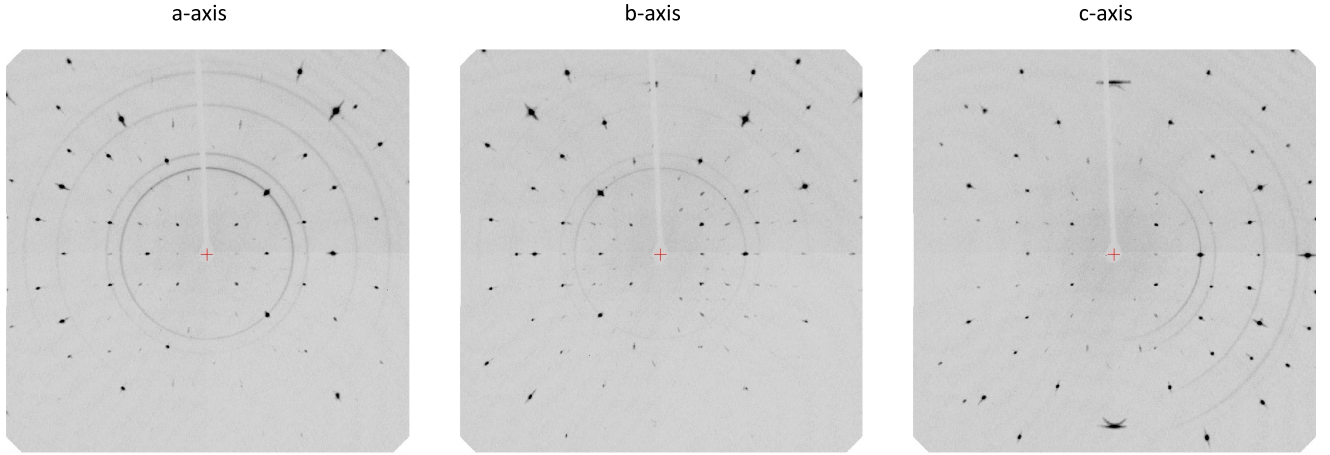


FIG. S1. X-ray diffraction images for the main crystal directions.

II. Magnetization

The T -dependence of the susceptibility M/H at 100 Oe is shown in Fig. S2a. The antiferromagnetic phase transition is clearly observed at 8.9 K. The high temperature curve can be fitted with a Curie-Weiss law²

$$M/H = \frac{C}{T - \Theta_{CW}} + \chi_0, \quad (\text{S1})$$

where C is the Curie constant, Θ_{CW} the Curie temperature and χ_0 is the T -independent part of the susceptibility (e.g. Van-Vleck susceptibility). There is an apparent change of slope around 40 K and additional susceptibility contribution below, the origin of which is unclear. It might stem from residual secondary GdPt₂ phase, which becomes ferromagnetic around 36-46.5 K¹. With $C = 1.571 \times 10^{-6} g^2 J(J+1)$ ², the effective moment can be estimated. The fit of the high-temperature susceptibility yields $6.86 \mu_B$, which is lower than the value of free Gd³⁺ ions ($7.94 \mu_B$ with $g = 2$ and $J = 7/2$), but roughly agrees with the reported values for GdPtBi³. Fitting the susceptibility down to lower temperatures yields higher values for the effective moment. The Curie temperature is extracted to $\Theta = -33 \text{ K}$, consistent with previous reports⁴⁻⁶ and indicating the frustration of the underlying Gd-lattice⁷. Below 2.5 K a slight upturn of the susceptibility is observed, which indicates the presence of paramagnetic impurities.

The magnetization M versus H is shown in Fig. S2b (left axis) at 2 K. A non-linearity around zero field is observed, better visible in the derivative shown in Fig. S2b (right axis). This non-linearity has also been observed in ref. 3 and is a clear deviation from an ideal antiferromagnet.

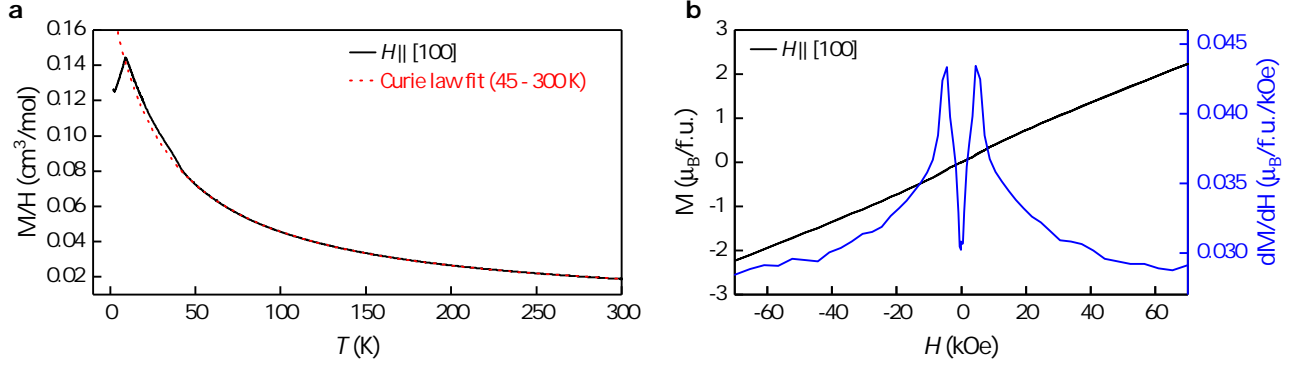


FIG. S2. a) Molar susceptibility M/H versus T of our GdPtBi sample. The dotted lines shows a fit with Eq. S1 from 45 to 300 K. b) Left axis: Magnetization M versus applied field H at 2 K. Right axis: Derivative of the $M(H)$ -curve.

III. *Ab-initio* band structure calculations

The DFT based first principles calculations were performed using the code of Vienna *ab-initio* simulation package (VASP) with the projected augmented wave method^{8,9}. The exchange and correlation energies were considered in the generalized gradient approximation (GGA) with the Perdew-Burke-Ernzerhof-based density functional¹⁰. The f -electrons in Gd were considered as the core state. We have projected the Bloch wavefunctions into the maximally localized Wannier functions (MLWFs)¹¹ and constructed the effective tight binding model Hamiltonian.

Our model revealed a triply degenerated point in GdPtBi near the Γ -point. To check, whether the anomalous magnetotransport features are related to this triple point crossing, we calculated the band structure for the non-magnetic YPtBi accordingly. A similar triple point is found for YPtBi, yet there have been no signatures of anomalous magnetotransport reported for YPtBi¹².

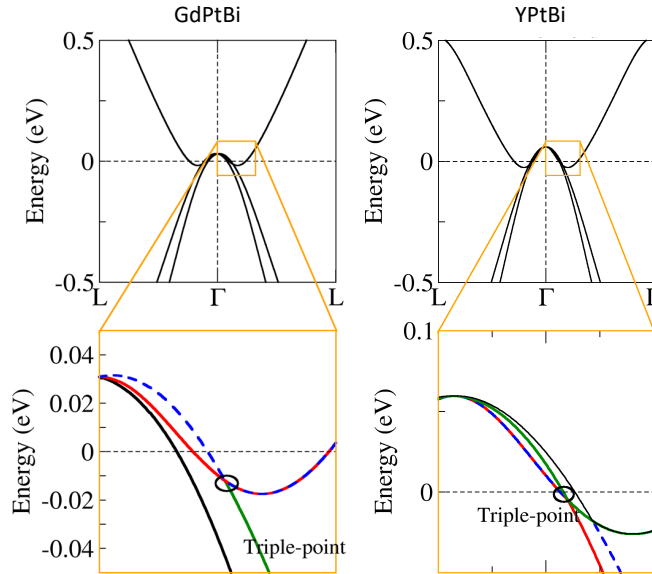


FIG. S3. Triple points along the $\Gamma - \text{L}$ -line in GdPtBi and YPtBi from DFT.

IV. Two-carrier transport

Above 10 K, $\rho(T)$ can be described with the two-carrier model¹³ of a narrow-gap material, where one carrier type gets thermally activated across an excitation gap. The total number of carriers is modeled as¹³

$$n(T) = n_0 + N \sqrt{k_B T \ln 2 [k_B T \ln(1 + e^{E_g/k_B T}) - E_g]}, \quad (\text{S2})$$

where n_0 is the number of temperature-independent carriers, N the density of states of the individual bands and E_g is the size of the bandgap. The resistivity then holds¹³

$$\rho(T) = \frac{\rho_0 n_0 + A \cdot T}{n(T)}, \quad (\text{S3})$$

where the term $A \cdot T$ accounts for the phonon scattering contribution, which is assumed to be linear above $\Theta_D/10$, where Θ_D is the Debye temperature. The fit is shown in Fig. 1a in the main text. The extracted E_g is 42 meV.

The Hall data was fitted with a two-carrier Drude model¹⁴

$$\rho_{xy} = \frac{1}{D} \left[R_1 \sigma_1^2 + R_2 \sigma_2^2 + R_1 R_2 \sigma_1^2 \sigma_2^2 (R_1 + R_2) H^2 \right], \quad (\text{S4})$$

with $D = (\sigma_1 + \sigma_2)^2 + (\sigma_1 \sigma_2)^2 (R_1 + R_2)^2 H^2$, where $\sigma_{1,2} = (nq\mu)_{1,2}$ are the Drude conductivities and $R_{1,2} = (1/qn)_{1,2}$ the Hall coefficients of the individual electron/hole channels. The extracted μ and n are shown in the insets in Fig. 1b in the main text.

The positive transverse MR at high T (see Fig. 3a in the main text) can partly be explained within the two-carrier model, where charge carrier compensation leads to a reduction of the Hall fields in relation to the size of the Lorentz forces. The two-carrier Drude model for the electrical MR holds¹⁴

$$\rho_{xx} = \frac{1}{D} \left[(\sigma_1 + \sigma_2)^2 + \sigma_1 \sigma_2 (\sigma_1 R_1^2 + \sigma_2 R_2^2) H^2 \right]. \quad (\text{S5})$$

Eq. S5 can reproduce the general features of the transverse MR-curves at high T consistent with the parameters extracted from the Hall data. However, at low T the electron density decreases significantly stronger than the hole density, which would also diminish carrier compensation effects and therefore cannot explain the large unsaturated transverse MR, which was shown to persist up to 600 kOe³. This effect might be explained in terms of field-dependent scattering times.

The electronic thermal conductivity of a two-carrier system in a transverse magnetic field holds¹⁴

$$\begin{aligned} \kappa_{xx} = \sum \kappa_{1,2} + \frac{T}{D} \left[\sigma_1 \sigma_2 (\sigma_1 + \sigma_2) (\Delta S_{1,2})^2 - \sigma_1 \sigma_2 \right. \\ \left. \times \Delta N_{1,2} [(\sigma_1 + \sigma_2) \Delta N_{1,2} - 2 \sigma_1 \sigma_2 \Delta S_{1,2} (R_1 + R_2)] H^2 \right], \end{aligned} \quad (\text{S6})$$

with $\sum \kappa_{1,2} = \kappa_1 + \kappa_2$ being the sum of the thermal conductivities of the individual channels. $\Delta S_{1,2} = S_1 - S_2$ and $\Delta N_{1,2} = N_1 - N_2$ are the differences of the individual Seebeck and Nernst coefficients, respectively. The H -dependent part of Eq. S6 yields a negative magnetothermal conductivity curve that is similar in shape to the inverse of Eq. S5.

V. Shubnikov-de-Haas oscillations

Shubnikov-de Haas oscillations (presumably of the hole pocket) in electrical resistivity were observed for low temperatures in both transverse and longitudinal \mathbf{H} -configuration (Figs. S4a,b). The oscillations were extracted by subtracting a smooth polynomial background from the ρ_{xx} -curve and plotting the residual versus inverse H . By fitting the resistivity maxima and minima, which correspond to filled and half-filled Landau levels N , respectively, with the linear function

$$N(1/H) = F/H + \beta, \quad (\text{S7})$$

we extracted the oscillation frequency F as 350 kOe for the transverse and 360 kOe for the longitudinal \mathbf{H} -configuration (see Figs. S4c,d). The oscillation frequency is connected to the Fermi surface area S_F via the Onsager relation¹⁵ $S_F = 2\pi e/\hbar F$, hence we can estimate a similar $S_F = (3.3 \pm 0.2) 10^{-3} \text{Å}^{-2}$ for both \mathbf{H} -configurations. Assuming

a circular Fermi surface, this gives the Fermi wave vector $k_F = \sqrt{S_F/\pi} = 0.033 \text{ \AA}^{-1}$. The volume of a spherical Fermi sea is then $V_F = 4/3 \times \pi k_F^3 = 1.43 \times 10^{-4} \text{ \AA}^{-3}$, which is less than 0.02% of the Brillouin zone volume $V_{\text{BZ}} = (2\pi/6.68)^3 \text{ \AA}^{-3} = 0.83 \text{ \AA}^{-3}$. The contribution of the electron pocket to the Fermi sea volume can be neglected for this estimation, since the electron density is about an order of magnitude lower than the hole density.

The phase shift β of the oscillations is 0.7 ± 0.1 for the transverse and 0.5 ± 0.1 for the longitudinal **H**-configuration.

From the T -dependent damping of the oscillation amplitude the effective mass m_{eff} can be extracted via¹⁵

$$\Delta\rho_{xx}(T) = \frac{\lambda(T)}{\sinh[\lambda(T)]}, \text{ with } \lambda(T) = 2\pi^2 \frac{m_{\text{eff}}}{eH} \frac{k_B T}{\hbar}, \quad (\text{S8})$$

where k_B is the Boltzmann constant and \hbar the reduced Planck constant. The T -dependent damping of $\Delta\rho_{xx}$ and the corresponding fit are shown in Fig. S4e. We extracted the effective mass to be $m_{\text{eff}} = (0.29 \pm 0.02)m_e$, with m_e being the electron rest mass. This result is comparable with that reported in refs. 3 and 16.

Lastly, we can extract the single-particle mobility μ_s from the $1/H$ -dependent damping of the oscillation amplitude via¹⁵

$$\Delta\rho_{xx}(1/B) = \exp\left[-\frac{\pi}{\mu_s H}\right]. \quad (\text{S9})$$

We extract the single-particle mobility of the hole pocket as $\mu_s = 1600 \pm 300 \text{ cm}^2 \text{V}^{-1} \text{s}^{-1}$. This value is much lower than the transport mobility extracted from the Hall analysis (see Fig. 1b in the main text), as the transport mobility is mostly dependent on momentum-relaxating scattering events whereas all collisions contribute equally to the single-particle mobility.

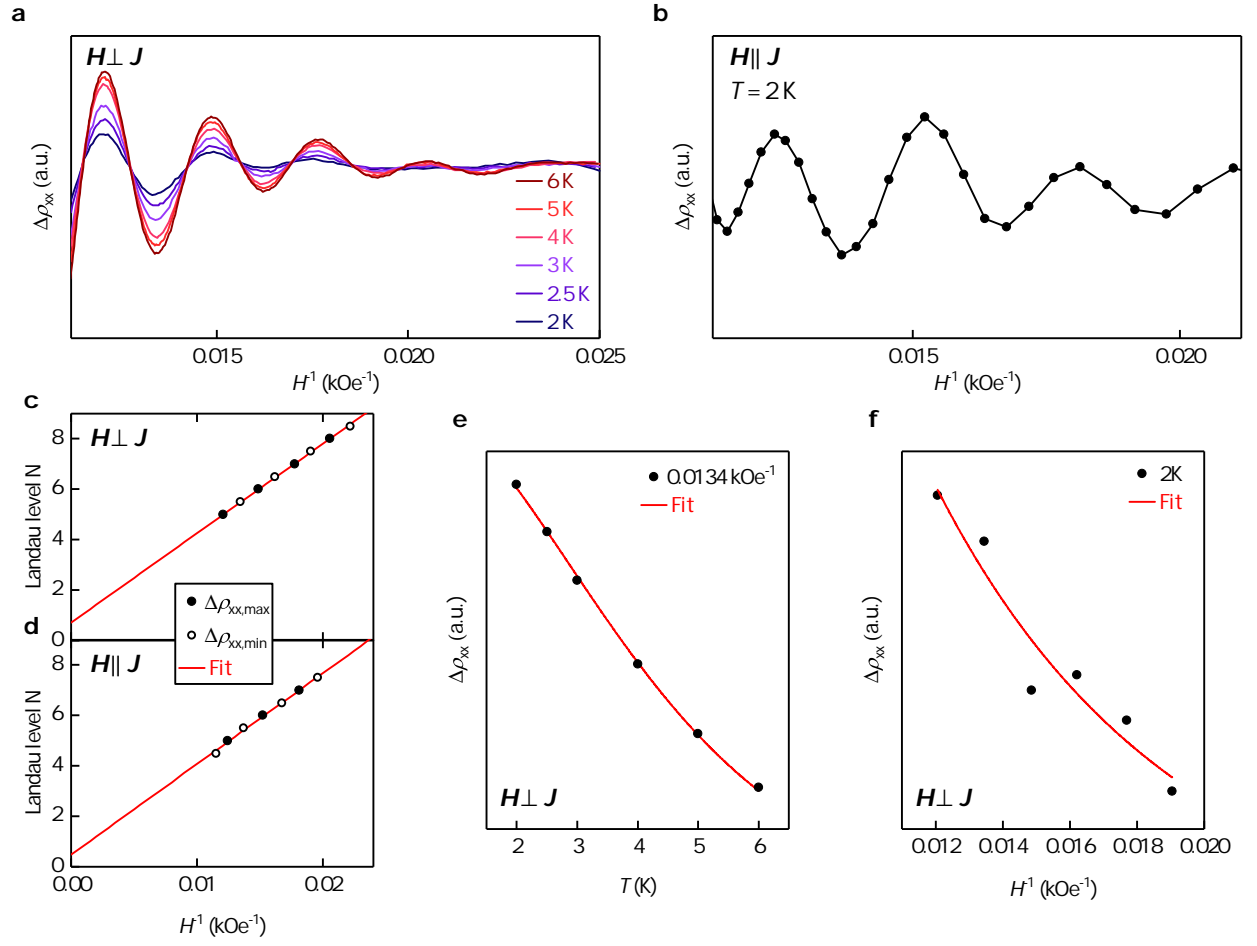


FIG. S4. Analysis of the Shubnikov-de-Haas (SdH) oscillations at low T . a,b) Extracted SdH oscillations vs. $1/H$ in transverse and longitudinal \mathbf{H} -configuration for different temperatures. c,d) Resistivity maxima and minima numerated by their corresponding Landau levels (LL) versus $1/H$. e) Oscillation amplitude at a fixed $1/H$ versus T . f) Oscillation amplitude at 2 K versus $1/H$. The solid line in (c-f) show the fits described in the text.

VI. Thermal transport measurements

For thermal measurements, four thermal contacts were fabricated (see Supplementary Figs. S5a,b). The contacts for the heater and for the heat sink were made by attaching gold-plated Cu-bars ($0.6 \times 0.25 \text{ mm}^2$) to the end faces of the sample using silver epoxy. The contacts for the two thermometers were made by wrapping 0.1 mm Pt-wire around the sample and subsequently fixating with silver epoxy to ensure low thermal contact resistance. For the heater, a $2 \text{ k}\Omega$ ruthenium oxide (Rox) thick-film resistor (type RX-202A) from Lake Shore¹⁷ was used and calibrated versus temperature (see Supplementary Fig. S5d). Rox resistors have an extremely low H -sensitivity, the error up to $H = 100 \text{ kOe}$ being less than 0.02% above $T = 30 \text{ K}$ ¹⁸. For the thermometers, two Cernox thin film resistors (type CX-1050) from Lake Shore¹⁹ were used. The thermometers were calibrated versus T (see Supplementary Fig. S5c) and versus H below $T = 16 \text{ K}$. Above $T = 30 \text{ K}$, the H -induced error of the Cernox thermometers is below 0.05% for $H < 100 \text{ kOe}$, decreasing significantly for higher temperatures²⁰. However, as for magnetothermal resistivity measurements we focus on the temperature difference ΔT between two similar thermometers, the H -induced error is even lower, because only a difference in the H -dependent behaviour would cause an error in ΔT .

The T -dependent thermal conductivity data in Fig. 2 was acquired using a continuous measurement mode, with a cooling rate of 0.25 K/min . Here, the heater was periodically turned on and off and κ is estimated from fitting the raw ΔT data for each heating/cooling period. The H -dependent thermal resistivity in Figs. 3(b,d) was acquired with steady-state measurements, where we wait for both thermometers to reach a stability criterion of $\delta T/T < 1 \text{ mK}$, before and after the heater had been turned on. This process lasted for up to an hour per data point.

As mentioned above, the H -induced error of the thermometers may still play a role if the thermometers would have different H -dependent behaviours. Therefore, we measured the H -dependency of the offset temperature difference ΔT_{offset} at zero heating power (see Supplementary Figs. S6a-d) and subsequently subtracted it from the raw ΔT data (Supplementary Figs. S6e,f). As further proof, we note that the qualitative behaviour of the offset does not significantly differ for the two \mathbf{H} -configurations. Additionally, the H -dependent change in ΔT_{offset} is more than one order of magnitude lower than the change in ΔT . Above 50 K , a significant H -dependence of this offset was not observed.

Moreover, we observed an increase of the absolute temperature of both thermometers with increasing H in both longitudinal and transverse configuration, by up to 0.22% at 90 kOe . Supplementary Fig. S7 shows the H -dependent change of the mean temperature T_{mean} of the two thermometers. This effect may either stem from the H -dependency of the thermometers or from magnetocaloric effects, which result in an actual rise of the sample temperature as H increases. To be on the safe side, we had to assume the latter, and thus estimated the systematic error of Δw_{xx} by multiplying the H -induced change of T_{mean} with the slope in $\kappa(T)$ for $T \pm 10 \text{ K}$. At 75 K , the increase of the sample temperature was the lowest, which guaranteed a low measurement error in thermal resistivity measurements at this temperature. In addition, we note that the qualitative behaviour of this effect was similar for both \mathbf{H} -configurations and can therefore be disregarded as an alternative reason for the observed anisotropy in thermal transport.

The statistic error of Δw_{xx} was estimated from the standard deviation of the two temperatures, and is approximately an order of magnitude lower than the systematic error. The combined error is shown as error bars in Figs. 3(b,d). We applied different heater power for each temperature curve, such that $\Delta T/T < 3\%$ (see Supplementary Figs. S6e,f).

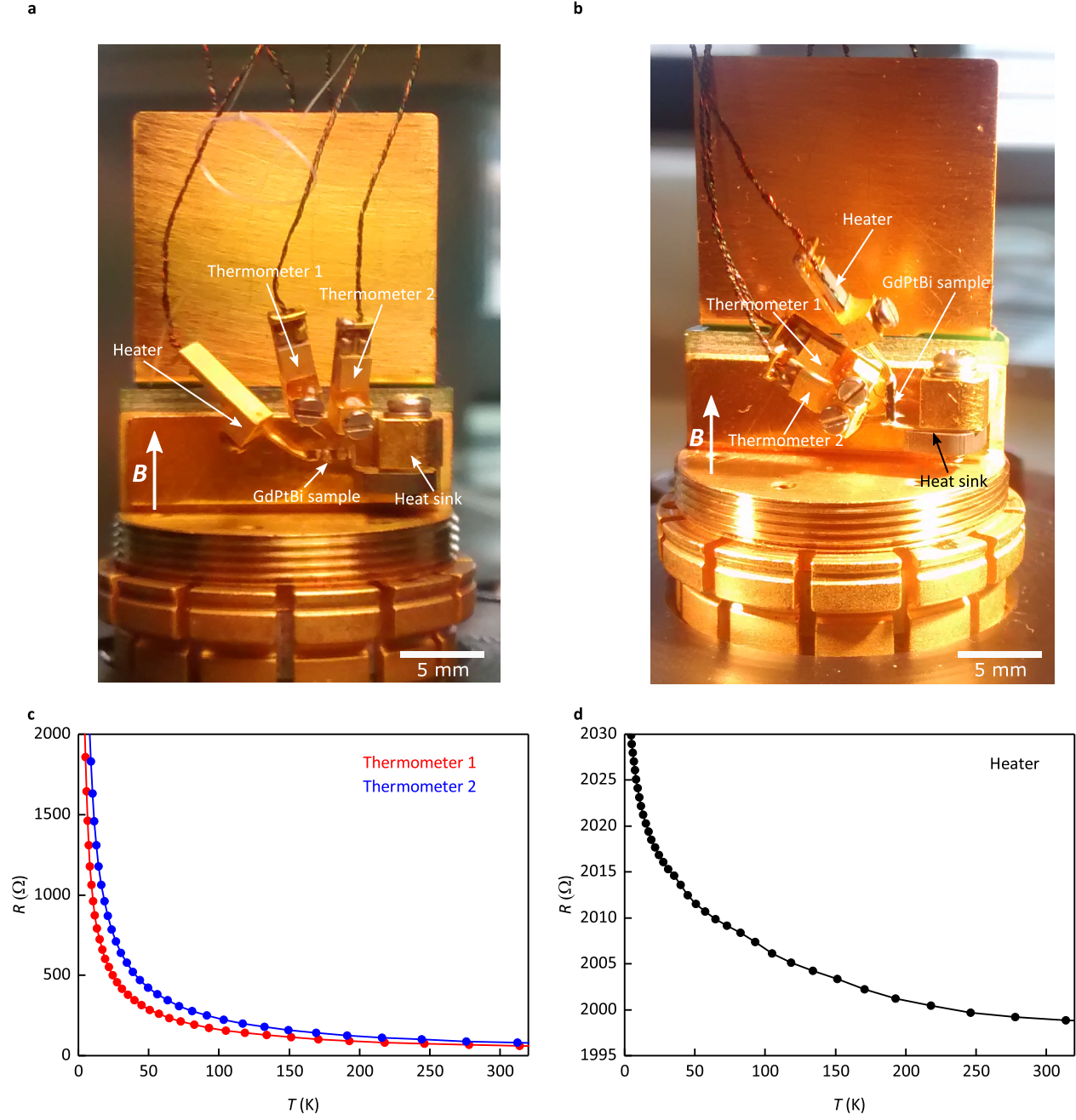


FIG. S5. Experimental setup for the thermal measurements and calibration curves. a)-b) Photographs of the thermal PUK with mounted sample in a) transverse and b) longitudinal \mathbf{B} -configuration. c) Resistance of the thermometers versus temperature curves. d) Heater resistance versus temperature. The curve between the data points in c) and d) is interpolated with a cubic spline.

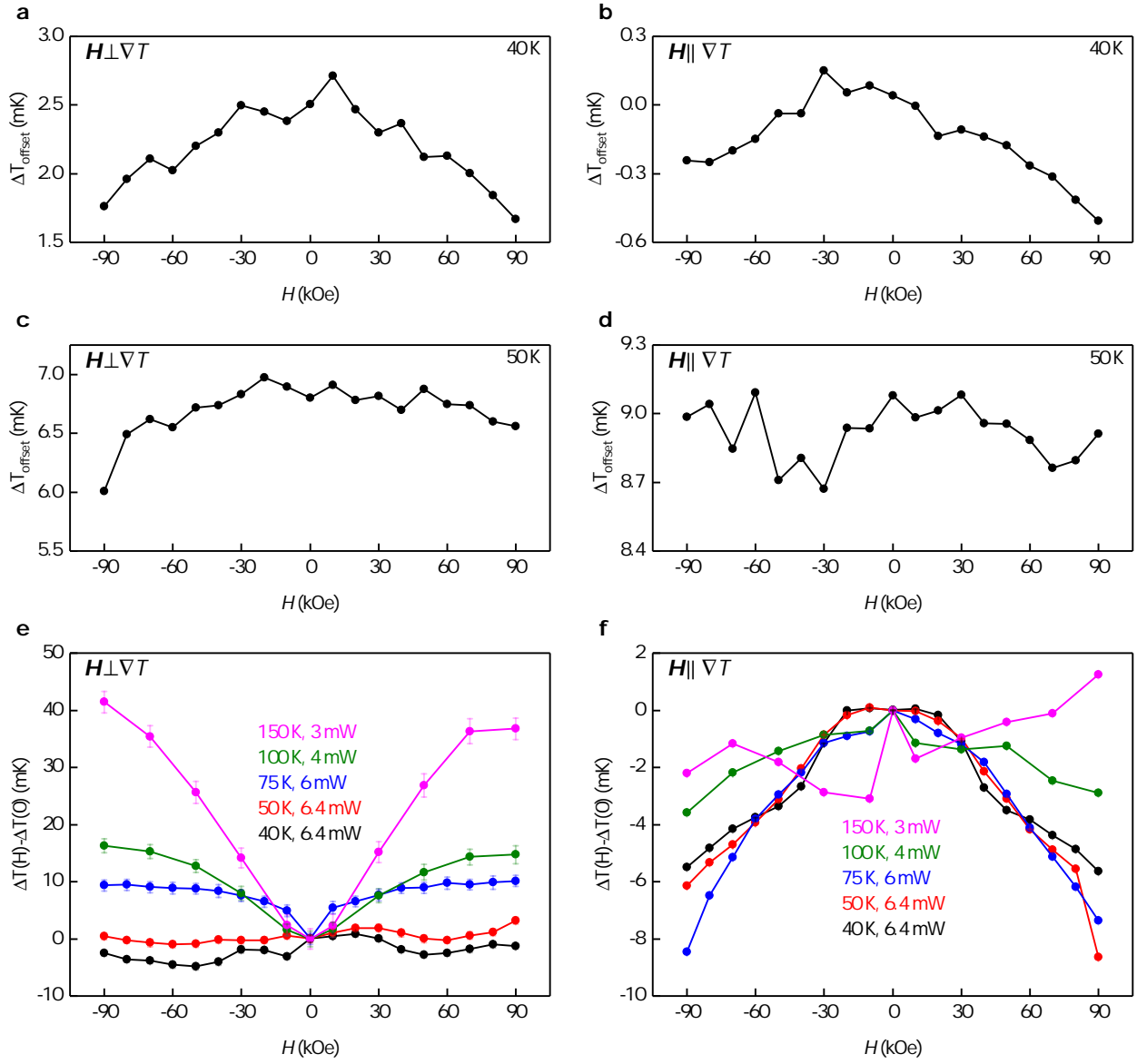


FIG. S6. Raw ΔT data versus H with and without applied heater power. a)-d) Temperature difference ΔT_{offset} without applying current to the heater versus H for transverse (a,c) and longitudinal (b,d) H -configuration at $T = 40$ K (a,b) and $T = 50$ K (c,d). e)-f) Raw data (without having removed the offset or symmetrized the data) of the H -induced change of ΔT for transverse (e) and longitudinal (f) H -configuration for fixed T and applied heater power.

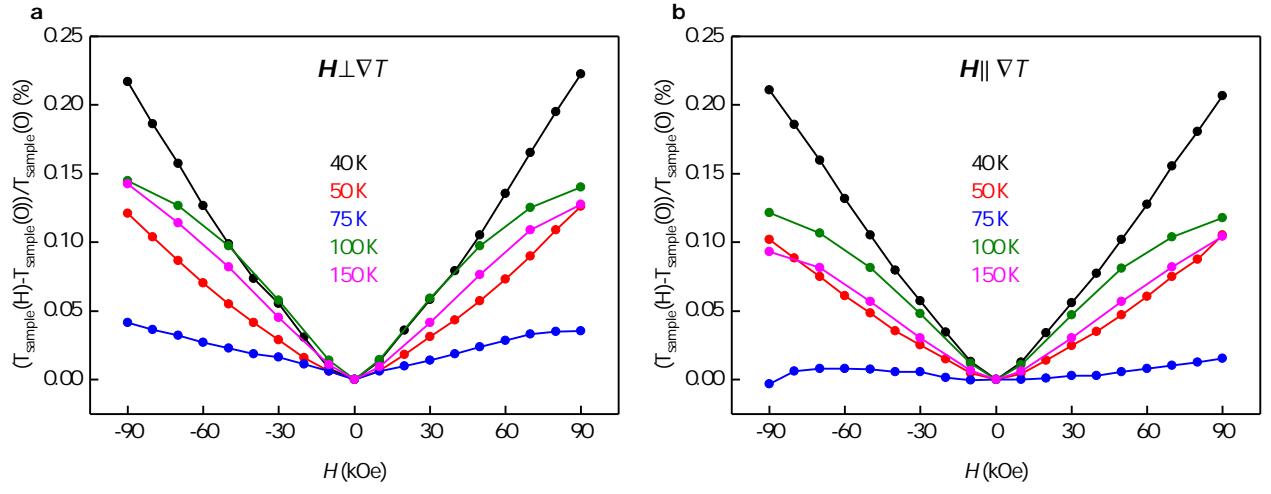


FIG. S7. Percent change of the mean temperature of the two thermometers vs. (a) transverse and (b) longitudinal H at fixed temperatures.

VII. Anomaly coefficient a_g in flat space-time.

In this section, we will derive how transport coefficients inherit a dependence on the mixed axial-gravitational anomaly coefficient a_g . This derivation is based on the observation that the energy current \mathbf{J}_ϵ , which has been derived using a Kubo approach to response coefficients, takes the form²¹

$$\mathbf{J}_\epsilon(\mu, T) = \left(\frac{1}{2} a_c \mu^2 + a_g T^2 \right) \mathbf{B} \quad (\text{S10})$$

for a right-handed node, and depends on its chemical potential μ , its temperature T and the two anomaly coefficients introduced in the main text (explicit expressions will be presented below).

In what follows we briefly review the theoretical arguments that motivate the above expression and its connection to the gravitational anomaly (a succinct, nearly self-contained account can be found in ref. 22). Firstly it is worth noting that Eq. S10 can be obtained from a Sommerfeld integral, typically used to calculate energy currents in flat space-time, without the need to refer to an anomaly. The first hint that these integrals “know” about the anomaly is the one to one mapping that exists between the generating functional of Sommerfeld integrals, like those leading to Eq. S10, and the anomaly generating functional^{22,23}. This intriguing mapping is suggestive of a deep connection between energy currents and gravitational anomalies^{21–28}.

The first support for this intuition was the observation based on a Kubo formula approach²¹, wherein the coefficient a_g appears both in the gravitational contribution to the chiral anomaly and transport coefficients in flat space-time. The identification was possible because a_g and a_c are anomaly coefficients determined by specific combinations of symmetry generators of the Lie group (explicit expressions will follow in the next appendix). Additional support for this observation was also found within global anomaly considerations^{24–26}, hydrodynamic accounts²⁷ and in an AdS/CFT setting²⁸.

Remarkably, ref. 22 found a physical set-up where the connection between the mixed axial-gravitational anomaly is explicitly linked to energy transport in flat space-times. As a *gedanken* experiment, consider a universe of Weyl fermions with a black hole. The space-time around the black hole is curved, and the anomalous non-conservation of the energy-momentum tensor due to the mixed axial-gravitational anomaly (and hence resulting from that curvature) has the physical interpretation of Hawking radiation (of Weyl fermions). The spectrum of this radiation is set by the Hawking temperature, which is in turn set by the space-time curvature. Now consider a flat region of space-time that is asymptotically far from the black hole. The energy current coming from the black hole continues to flow into the flat space-time region. In doing so, it will maintain its temperature, the Hawking temperature. Thus, energy transport at a given temperature in flat space-time has to be smoothly connected to energy transport in curved space-times upon replacing temperature by the Hawking temperature, which is set by space-time curvature, and is hence linked to the mixed axial-gravitational anomaly.

A last, indirect reason for the plausibility of the connection discussed by the above works is that a_c , the well known coefficient for the electromagnetic contribution to the chiral anomaly, sets the constitutive (zero field!) parameters of hydrodynamic quantities to avoid an unphysical entropy growth due to a finite $\mathbf{E} \cdot \mathbf{B}$ ^{22,29}. Thus it is not unlikely that there exists a consistency condition that fixes a_g to appear even in the absence of curvature.

We note that semiclassical theory can also be used to calculate transport coefficients. Provided one takes into account the Berry phase to include topological effects, this procedure yields the correct result. However, it simply does not keep track of the fact that some terms in the transport equations are related to anomaly coefficients. The semiclassical approach is therefore “blind” to this connection.

VIII. Expressions for transport coefficients.

In applied electromagnetic fields and curved space-time, the energy-momentum tensor and the chiral current vector are not conserved for individual Weyl nodes. The anomalous non-conservation of the mixed axial current $J_A^\mu = J_R^\mu - J_L^\mu$ is described by the anomalous continuity equations

$$\partial_\mu J_A^\mu = \frac{d_{AVV}}{32\pi^2} \epsilon^{\mu\nu\rho\sigma} F_{\mu\nu}^\nu F_{\rho\sigma}^\nu + \frac{b_A}{768\pi^2} \epsilon^{\mu\nu\rho\sigma} R_{\beta\mu\nu}^\alpha R_{\alpha\rho\sigma}^\beta, \quad (\text{S11})$$

where $J_{R(L)}^\mu$ is the current four-vector associated with a Weyl node of right-handed (left-handed) chirality. Hereafter, we distinguish between mixed axial quantities (which have different signs for nodes of different chiralities), and vector quantities (which have the same sign for nodes of different chiralities). As an example, $F_{\mu\nu}^\nu$ is the vector field strength tensor: the field strength that couples symmetrically to nodes of either chirality (the components of $F_{\mu\nu}^{(V)}$ are the

usual electromagnetic fields). In addition, $R^\alpha_{\beta\mu\nu}$ denotes the Riemann space-time curvature tensor, while d_{AVV} and b_{A} are the so-called “anomaly coefficients” which will be linked to a_{c} and a_{g} , respectively, shortly.

The anomaly coefficients physically encode the “ability” of a given physical system to show quantum anomalies when the system is exposed to appropriate conditions, such as applied electromagnetic fields and curved space-times. The present work does not measure the anomalous non-conservation of chiral charge in curved space-time (the space-time is flat!), but rather the anomaly coefficient b_{A} (shortly a_{g}) associated with the mixed axial-gravitational anomaly. The anomaly coefficients are set by the symmetries of the chiral fermions; if a given species of chiral fermions transforms under a Lie group generated by matrices T^α (for example in the presence of the gauge field of the electromagnetic field), the anomaly coefficients are given by

$$d_{\alpha\beta\gamma} = \frac{1}{2} \left(\text{tr}(T_\alpha \{T_\beta, T_\gamma\})_{\text{L}} - \text{tr}(T_\alpha \{T_\beta, T_\gamma\})_{\text{R}} \right), \quad (\text{S12a})$$

$$b_\alpha = \text{tr}(T_\alpha)_{\text{L}} - \text{tr}(T_\alpha)_{\text{R}}, \quad (\text{S12b})$$

where the sums run over the species of left (L)- and right- (R) handed fermions and $\{\cdot, \cdot\}$ is the anti-commutator (see ref. 24 for a pedagogical introduction).

In the following, we provide a simple relaxation-time calculation that explains how anomaly coefficients appear in transport. This calculation is an extension of the calculations discussed in refs. 30 and 31. We specialize to a system that has two Weyl nodes of opposite chirality. For any quantity O_χ , associated with a node of chirality $\chi = \text{R, L}$, we define the vector quantity O_{V} and the mixed axial quantity O_{A} as

$$O_{\text{V}} = O_{\text{R}} + O_{\text{L}} \quad \text{and} \quad O_{\text{A}} = O_{\text{R}} - O_{\text{L}}. \quad (\text{S13})$$

This implies that

$$O_{\text{R}}^2 + O_{\text{L}}^2 = \frac{1}{2} (O_{\text{V}}^2 + O_{\text{A}}^2) \quad \text{and} \quad O_{\text{R}}^2 - O_{\text{L}}^2 = O_{\text{V}} O_{\text{A}}. \quad (\text{S14})$$

In the following, we calculate the magnetic field-dependent contribution to the particle currents \mathbf{J}_χ and energy currents $\mathbf{J}_{\epsilon, \chi}$ for Weyl fermions of chirality χ . As discussed in ref. 32, the standard Kubo formalism for Weyl fermions leads to

$$\mathbf{J}_\chi(\mu_\chi, T_\chi) = \hat{\chi} a_{\text{c}} \mu_\chi \mathbf{B}, \quad (\text{S15a})$$

$$\mathbf{J}_{\epsilon, \chi}(\mu_\chi, T_\chi) = \hat{\chi} \left(\frac{1}{2} a_{\text{c}} \mu_\chi^2 + a_{\text{g}} T_\chi^2 \right) \mathbf{B}, \quad (\text{S15b})$$

with $\hat{\chi}$ taking the values $\hat{R} = +1$ and $\hat{L} = -1$. Note that the introduction of a well-defined chemical potential μ_χ and temperature T_χ for the node of chirality χ implies that the intra-node scattering times are much shorter than inter-node scattering times. In these expressions, a_{c} and a_{g} are the anomaly coefficients of the chiral and mixed axial-gravitational anomaly, renormalized by universal factors for the sake of simplifying the subsequent equations,

$$a_{\text{c}} = \hat{\chi} \frac{e}{4\pi^2 \hbar^2} d_{\alpha\beta\gamma}, \quad (\text{S16})$$

$$a_{\text{g}} = \hat{\chi} \frac{ek_{\text{B}}^2}{24\hbar^2} b_\alpha. \quad (\text{S17})$$

While charge and energy are not conserved at a given individual Weyl node due to the chiral and mixed axial-gravitational anomalies, the total charge and energy have to be conserved in a solid. As a result, the total charge density and the total energy density obey the following continuity equations:

$$\dot{\rho}_{\text{V}} + \nabla \cdot \mathbf{J}_{\text{V}} = 0 \quad \text{and} \quad \dot{\rho}_{\epsilon, \text{V}} + \nabla \cdot \mathbf{J}_{\epsilon, \text{V}} = 0, \quad (\text{S18})$$

where $\rho_{\text{V}} = \rho_{\text{R}} + \rho_{\text{L}}$ is the total charge density, and $\rho_{\epsilon, \text{V}} = \rho_{\epsilon, \text{R}} + \rho_{\epsilon, \text{L}}$ is the total energy density. In the steady state, we thus have

$$0 = \nabla \cdot \mathbf{J}_{\text{V}} = \nabla \cdot (a_{\text{c}} \mu_{\text{A}} \mathbf{B}). \quad (\text{S19})$$

For a system with a constant and homogeneous magnetic field, this implies that

$$\nabla \mu_{\text{A}} = 0. \quad (\text{S20})$$

Additionally, at finite chemical potential we may assume

$$\nabla \mu_V = 0. \quad (\text{S21})$$

Combined with Eq. (S20), this translates into assuming $\nabla \mu_R = 0 = \nabla \mu_L$, and hence constant chemical potentials inside the system for both chiralities. Note that this condition can still be satisfied even if $\mu_R \neq \mu_L$. In the steady state, the continuity equation for the energy density furthermore implies

$$0 = \nabla \cdot \mathbf{J}_{\epsilon,V} = \nabla \cdot \left(\frac{1}{2} a_c \mu_V \mu_A + a_g T_V T_A \right) \mathbf{B}. \quad (\text{S22})$$

For constant magnetic field, and using Eqs. (S20) and (S21), this implies

$$\nabla (T_A T_V) = 0 \quad \Rightarrow \quad \nabla T_A = -\frac{T_A}{T_V} \nabla T_V. \quad (\text{S23})$$

With this, we can now come to the vector current densities. Their k^{th} component satisfies

$$\begin{pmatrix} J_{V,k} \\ J_{\epsilon,V,k} \end{pmatrix} = \begin{pmatrix} a_c & 0 \\ \frac{1}{2} a_c \mu_V & a_g T_V \end{pmatrix} \begin{pmatrix} \mu_A \\ T_A \end{pmatrix} B_k. \quad (\text{S24})$$

To find μ_A and T_A , we use their anomalous continuity equations. For the mixed axial particle current, and using $j_\chi \sim \mu_\chi$ and $\nabla \mu_\chi = 0$ (see above), we have

$$\dot{\rho}_A = 2 e a_c \mathbf{E} \cdot \mathbf{B}. \quad (\text{S25})$$

Similarly, the mixed axial energy current density obeys

$$\dot{\rho}_{\epsilon,A} + \nabla \cdot \mathbf{J}_{\epsilon,A} = e \mathbf{J}_A \cdot \mathbf{E}. \quad (\text{S26})$$

For the divergence of the mixed axial energy current density, we find

$$\nabla \cdot \mathbf{J}_{\epsilon,A} = \nabla \cdot \left(\frac{1}{2} a_c \frac{\mu_V^2 + \mu_A^2}{2} + a_g \frac{T_V^2 + T_A^2}{2} \right) \mathbf{B}. \quad (\text{S27})$$

Using Eqs. (S21) and (S20), this implies

$$\nabla \cdot \mathbf{J}_{\epsilon,A} = a_g (T_V \nabla T_V + T_A \nabla T_A) \cdot \mathbf{B}. \quad (\text{S28})$$

Using Eq. (S23), this in turn leads to

$$\nabla \cdot \mathbf{J}_{\epsilon,A} = a_g \left(T_V \nabla T_V - \frac{T_A^2}{T_V^2} T_V \nabla T_V \right) \cdot \mathbf{B}. \quad (\text{S29})$$

Physically, we want to specialize to the linear response regime in which

$$T_A \ll T_V, \quad (\text{S30})$$

and hence

$$\nabla \cdot \mathbf{J}_{\epsilon,A} \approx a_g T_V \nabla T_V \cdot \mathbf{B}. \quad (\text{S31})$$

Next, we add some physical insight into these equations. Namely, we expect that the mixed axial particle and energy densities, created by the chiral anomaly, relax back to their equilibrium values $\rho_A = 0 = \rho_{\epsilon,A}$ due to inter-node scattering. We model this by adding relaxation times τ for mixed axial densities and τ_ϵ for mixed axial energy densities to the continuity equations:

$$\dot{\rho}_A \approx 2 a_c \mathbf{E} \cdot \mathbf{B} - \frac{\rho_A}{\tau}, \quad (\text{S32a})$$

$$\dot{\rho}_{\epsilon,A} \approx -a_g T_V \nabla T_V \cdot \mathbf{B} + e \mathbf{J}_A \cdot \mathbf{E} - \frac{\rho_{\epsilon,A}}{\tau_\epsilon}. \quad (\text{S32b})$$

In the steady state, and using Eq. (S15), we find

$$\begin{pmatrix} \rho_A \\ \rho_{\epsilon,A} \end{pmatrix} \approx \begin{pmatrix} 2\tau e a_c & 0 \\ \tau_e e a_c \mu_V & -\tau_e a_g T_V \end{pmatrix} \begin{pmatrix} \mathbf{E} \cdot \mathbf{B} \\ \nabla T_V \cdot \mathbf{B} \end{pmatrix}. \quad (\text{S33})$$

In order to calculate the conductivities, we still need a relation between the mixed axial densities, the mixed axial chemical potential, and the mixed axial temperature. We thus turn to the particle and energy densities for a node of chirality χ . We demand that the nodes are identical except for their chirality. In that case, the particle and energy densities for a node of chirality χ only depend on its effective chemical potential μ_χ and its effective temperature T_χ , but not directly on the chirality:

$$\rho_\chi(\mu_\chi, T_\chi) = \rho(\mu_\chi, T_\chi) \quad \text{and} \quad \rho_{\epsilon,\chi}(\mu_\chi, T_\chi) = \rho_\epsilon(\mu_\chi, T_\chi), \quad (\text{S34})$$

where $\rho(\rho_\epsilon)$ is the particle (energy) density of one Weyl node. Since $\mu_\chi = (\mu_V + \mu_A)/2$ and $T_\chi = (T_V + T_A)/2$, we find for $\mu_V \gg \mu_A$ and $T_V \gg T_A$ that

$$\begin{aligned} \rho_\chi(\mu_\chi, T_\chi) &\approx \rho\left(\frac{\mu_V}{2}, \frac{T_V}{2}\right) + \frac{\partial \rho\left(\frac{\mu_V}{2}, \frac{T_V}{2}\right)}{\partial \mu} \hat{\chi} \frac{\mu_A}{2} + \frac{\partial \rho\left(\frac{\mu_V}{2}, \frac{T_V}{2}\right)}{\partial T} \hat{\chi} \frac{T_A}{2}, \\ \rho_{\epsilon,\chi}(\mu_\chi, T_\chi) &\approx \rho_\epsilon\left(\frac{\mu_V}{2}, \frac{T_V}{2}\right) + \frac{\partial \rho_\epsilon\left(\frac{\mu_V}{2}, \frac{T_V}{2}\right)}{\partial \mu} \hat{\chi} \frac{\mu_A}{2} + \frac{\partial \rho_\epsilon\left(\frac{\mu_V}{2}, \frac{T_V}{2}\right)}{\partial T} \hat{\chi} \frac{T_A}{2}. \end{aligned}$$

The mixed axial densities thus satisfy

$$\begin{pmatrix} \rho_A \\ \rho_{\epsilon,A} \end{pmatrix}_{\mu_V/2, T_V/2} \approx \begin{pmatrix} \partial_\mu \rho & \partial_T \rho \\ \partial_\mu \rho_\epsilon & \partial_T \rho_\epsilon \end{pmatrix}_{\mu_V/2, T_V/2} \begin{pmatrix} \mu_A \\ T_A \end{pmatrix}. \quad (\text{S35})$$

To put everything together, we define “the system’s temperature T ” as the average temperature of the two chiralities, and “the system’s chemical potential μ ” as the average chemical potential,

$$\mu = \frac{\mu_R + \mu_L}{2} = \frac{\mu_V}{2} \quad \text{and} \quad T = \frac{T_R + T_L}{2} = \frac{T_V}{2}. \quad (\text{S36})$$

Combining Eqs. (S24), (S33) and (S35), we obtain the k^{th} component of the vector (=total) particle current density and vector (=total) energy current density, the mixed axial chemical potential and mixed axial temperature, and the mixed axial particle density and mixed axial energy density as

$$\begin{pmatrix} J_{V,k} \\ J_{\epsilon,V,k} \end{pmatrix}_{\mu,T} \approx 2 \begin{pmatrix} a_c & 0 \\ a_c \mu & 2 a_g T \end{pmatrix} \begin{pmatrix} \partial_\mu \rho & \partial_T \rho \\ \partial_\mu \rho_\epsilon & \partial_T \rho_\epsilon \end{pmatrix}_{\mu,T}^{-1} \begin{pmatrix} \tau e a_c & 0 \\ \tau_e e a_c \mu & -2 \tau_e a_g T \end{pmatrix} \begin{pmatrix} \mathbf{E} \cdot \mathbf{B} \\ \nabla T \cdot \mathbf{B} \end{pmatrix} B_k, \quad (\text{S37})$$

$$\begin{pmatrix} \mu_A \\ T_A \end{pmatrix}_{\mu,T} \approx 2 \begin{pmatrix} \partial_\mu \rho & \partial_T \rho \\ \partial_\mu \rho_\epsilon & \partial_T \rho_\epsilon \end{pmatrix}_{\mu,T}^{-1} \begin{pmatrix} \tau e a_c & 0 \\ \tau_e e a_c \mu & -2 \tau_e a_g T \end{pmatrix} \begin{pmatrix} \mathbf{E} \cdot \mathbf{B} \\ \nabla T \cdot \mathbf{B} \end{pmatrix}, \quad (\text{S38})$$

$$\begin{pmatrix} \rho_A \\ \rho_{\epsilon,A} \end{pmatrix}_{\mu,T} \approx 2 \begin{pmatrix} \tau e a_c & 0 \\ \tau_e e a_c \mu & -2 \tau_e a_g T \end{pmatrix} \begin{pmatrix} \mathbf{E} \cdot \mathbf{B} \\ \nabla T \cdot \mathbf{B} \end{pmatrix}. \quad (\text{S39})$$

The explicit expressions for the total currents can be evaluated at a given magnetic field strength upon summing up the particle and energy densities of all occupied states (Landau levels). In the limit of very small or very large fields, this calculation can be performed analytically. We assume a homogeneous Fermi velocity v_F . In the case of small magnetic fields, the system behaves as a gas of free Weyl fermions. For a node of chirality χ , the energy density is then given by

$$\lim_{|\mathbf{B}| \rightarrow 0} \rho_{\epsilon,\chi}(\mu_\chi, T_\chi) = \frac{1}{8\pi^2 v_F^3 \hbar^3} \left(\mu_\chi^4 + 2\pi^2 k_B^2 T_\chi^2 \mu_\chi^2 + \frac{7}{15} \pi^4 k_B^4 T_\chi^4 \right) \quad (\text{S40})$$

(see for instance ref. 33). For large magnetic fields, the system splits into degenerate one-dimensional systems, the number of which is set by the Landau level degeneracy. In this case, the energy density reads

$$\lim_{|\mathbf{B}| \rightarrow \infty} \rho_{\epsilon,\chi}(\mu_\chi, T_\chi) = \frac{e|\mathbf{B}|}{8\pi^2 \hbar^2 v_F} \left(\mu_\chi^2 + \frac{\pi}{3} k_B^2 T_\chi^2 \right). \quad (\text{S41})$$

For small and large magnetic fields, the particle densities are given respectively by

$$\lim_{|\mathbf{B}| \rightarrow 0} \rho_\chi(\mu_\chi, T_\chi) = \mu_\chi \frac{\mu_\chi^2 + \pi^2 k_B^2 T_\chi^2}{6\pi^2 v_F^3 \hbar^3}, \quad (\text{S42})$$

$$\lim_{|\mathbf{B}| \rightarrow \infty} \rho_\chi(\mu_\chi, T_\chi) = \frac{e|\mathbf{B}|}{4\pi^2 \hbar^2 v_F} \mu_\chi. \quad (\text{S43})$$

Calculating $\partial_\mu \rho$, $\partial_T \rho$, $\partial_\mu \rho_\epsilon$, and $\partial_T \rho_\epsilon$, we obtain the i^{th} component of the total current density $\mathbf{J} = \mathbf{J}_V$ and the total energy current density $\mathbf{J}_\epsilon = \mathbf{J}_{\epsilon,V}$. For the components of the vector current, this allows us to define the response coefficients G^{ij} , G_T^{ij} , G_ϵ^{ij} , and $G_{\epsilon,T}^{ij}$

$$J_i(\mu, T) = G^{ij} E_j + G_T^{ij} (-\nabla_j T) \quad (\text{S44})$$

$$J_{\epsilon,i}(\mu, T) = G_\epsilon^{ij} E_j + G_{\epsilon,T}^{ij} (-\nabla_j T). \quad (\text{S45})$$

1. Limit $\mathbf{B} \rightarrow 0$

In the limit $\mathbf{B} \rightarrow 0$, we find

$$\lim_{|\mathbf{B}| \rightarrow 0} G^{ij} = a_c^2 \frac{12\pi^2 v_F^3 \hbar^3 e (7\pi^2 k_B^2 T^2 \tau + 5\mu^2 (3\tau - 2\tau_\epsilon))}{7\pi^4 k_B^4 T^4 + 6\pi^2 k_B^2 T^2 \mu^2 + 15\mu^4} B_i B_j, \quad (\text{S46})$$

$$\lim_{|\mathbf{B}| \rightarrow 0} G_T^{ij} = -a_c a_g \frac{240\pi^2 v_F^3 \hbar^3 T \tau_\epsilon}{7\pi^4 k_B^4 T^4 + 6\pi^2 k_B^2 T^2 \mu^2 + 15\mu^4} \mu B_i B_j, \quad (\text{S47})$$

$$\begin{aligned} \lim_{|\mathbf{B}| \rightarrow 0} G_\epsilon^{ij} = & a_c^2 \frac{12\pi^2 v_F^3 \hbar^3 e (7\pi^2 k_B^2 T^2 \tau + 5\mu^2 (3\tau - 2\tau_\epsilon))}{7\pi^4 k_B^4 T^4 + 6\pi^2 k_B^2 T^2 \mu^2 + 15\mu^4} \mu B_i B_j \\ & + a_c \frac{a_g}{k_B^2} \frac{120v_F^3 \hbar^3 e (\pi^2 k_B^2 T^2 (\tau_\epsilon - 3\tau) + 3\mu^2 (\tau_\epsilon - \tau))}{7\pi^4 k_B^4 T^4 + 6\pi^2 k_B^2 T^2 \mu^2 + 15\mu^4} \mu B_i B_j, \end{aligned} \quad (\text{S48})$$

$$\lim_{|\mathbf{B}| \rightarrow 0} G_{\epsilon,T}^{ij} = \frac{a_g}{k_B^2} \frac{240v_F^3 \hbar^3 T \tau_\epsilon (\mu^2 (3a_g - \pi^2 a_c k_B^2) + \pi^2 a_g k_B^2 T^2)}{7\pi^4 k_B^4 T^4 + 6\pi^2 k_B^2 T^2 \mu^2 + 15\mu^4} B_i B_j. \quad (\text{S49})$$

2. Limit $\mathbf{B} \rightarrow \infty$

In the large field limit, we have

$$\lim_{|\mathbf{B}| \rightarrow \infty} G^{ij} = a_c^2 8\pi^2 v_F \hbar^2 \tau \frac{B_i B_j}{|\mathbf{B}|}, \quad (\text{S50})$$

$$\lim_{|\mathbf{B}| \rightarrow \infty} G_T^{ij} = 0, \quad (\text{S51})$$

$$\lim_{|\mathbf{B}| \rightarrow \infty} G_\epsilon^{ij} = a_c 8v_F \hbar^2 \frac{(6a_g(\tau_\epsilon - \tau) + \pi^2 a_c k_B^2 \tau)}{k_B^2} \mu \frac{B_i B_j}{|\mathbf{B}|}, \quad (\text{S52})$$

$$\lim_{|\mathbf{B}| \rightarrow \infty} G_{\epsilon,T}^{ij} = a_g^2 \frac{96v_F \hbar^2 T \tau_\epsilon}{e k_B^2} \frac{B_i B_j}{|\mathbf{B}|}. \quad (\text{S53})$$

3. Transport coefficients

The electrical conductivity σ is defined as the response of an electrical current density \mathbf{J} to an electric field \mathbf{E} under isothermal conditions ($\nabla T = 0$). Thus, it holds

$$\sigma^{ij} = G^{ij}. \quad (\text{S54})$$

The thermoelectrical conductivity α is defined as the closed-circuit ($\mathbf{E} = 0$) response of an electric current \mathbf{J} to a temperature gradient $-\nabla T$. It holds

$$\alpha^{ij} = G_T^{ij}. \quad (\text{S55})$$

The Seebeck coefficient S is defined as the open-circuit ($\mathbf{J} = 0$) response of an electric field \mathbf{E} to a temperature gradient $-\nabla T$ and is thus defined as

$$S^{ij} = \frac{G_T^{ij}}{G_{ij}^{ij}}. \quad (\text{S56})$$

Hence, we obtain

$$\lim_{|\mathbf{B}| \rightarrow 0} S^{ij} = \frac{a_g}{a_c} \frac{20T\mu\tau_\epsilon}{e(7\pi^2 k_B^2 T^2 \tau + 15\mu^2 \tau - 10\mu^2 \tau_\epsilon)}, \quad (\text{S57})$$

$$\lim_{|\mathbf{B}| \rightarrow \infty} S^{ij} = 0 \quad (\text{S58})$$

The thermal conductivity κ is defined as the open-circuit ($\mathbf{J} = 0$) response of a heat current $\mathbf{J}_h = \mathbf{J}_\epsilon - \mu\mathbf{J}$ to a temperature gradient $-\nabla T$. Thus, it is obtained by setting Eq. (S44) to zero and inserting into Eq. (S45)

$$\kappa^{ij} = -G_\epsilon^{ij} \frac{G_T^{ij}}{G_{ij}^{ij}} + G_{\epsilon,T}^{ij}. \quad (\text{S59})$$

We obtain

$$\lim_{|\mathbf{B}| \rightarrow 0} \kappa^{ij} = a_g^2 \frac{240v_F^3 \hbar^3 T \tau \tau_\epsilon}{7\pi^2 k_B T^2 \tau + 5k_B \mu^2 (3\tau - 2\tau_\epsilon)} B_i B_j, \quad (\text{S60})$$

$$\lim_{|\mathbf{B}| \rightarrow \infty} \kappa^{ij} = a_g^2 \frac{96v_F \hbar^2 T \tau_\epsilon}{ek_B^2} \frac{B_i B_j}{|\mathbf{B}|}. \quad (\text{S61})$$

Setting $\tau = \tau_\epsilon$ and adding a Drude contribution, we obtain the functional forms used in the main text.

4. Comparison between theory and experiment

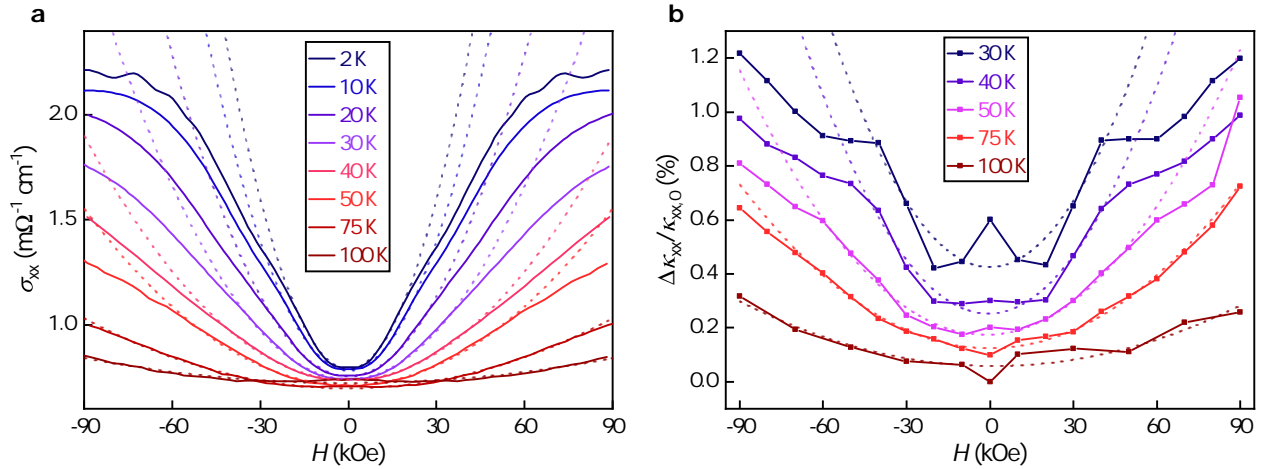


FIG. S8. Comparison between the predictions for the chiral magnetic effect and experiment. The dashed lines represent quadratic fits. a) Longitudinal conductivity $\sigma_{xx,\parallel} = 1/\rho_{xx,\parallel}$ versus magnetic field. b) Longitudinal thermal conductivity $\kappa_{xx,\parallel} = 1/w_{xx,\parallel}$ versus magnetic field. For better visibility the percental change is shown and the curves are shifted by a constant offset. Both thermal and electrical conductivities are proportional to H^2 in the low-field regime.

With $\rho_{xy} \approx 0$ and $w_{xy} \approx 0$ in the longitudinal configuration, the electrical and thermal conductivities can be calculated via $\sigma_{xx,\parallel} = 1/\rho_{xx,\parallel}$ and $\kappa_{xx,\parallel} = 1/w_{xx,\parallel}$. The predictions for the chiral magnetic effect for $\sigma_{xx,\parallel}$ and $\kappa_{xx,\parallel}$ hold in the low-field regime, where a proportionality to H^2 is observed (see Fig. S8). Interestingly, the field range, where the quadratic function fits, decreases with decreasing temperature in both electrical and thermal conductivities. For the quantum limit in high fields, a deviation towards a linear H -dependence is predicted for $\sigma_{xx,\parallel}$ and $\kappa_{xx,\parallel}$. For

$\sigma_{xx,\parallel}$, this deviation can be seen for temperatures above 40 K, however, for lower temperatures, $\sigma_{xx,\parallel}$ does not follow this prediction and rather seems to saturate at high fields. Similarly, $\kappa_{xx,\parallel}$ shows a clear deviation in slope around 40 kOe for temperatures below 50 K.

-
- * johannes.gooth@cpfs.mpg.de
- ¹ Buschow, K. J. H. Intermetallic compounds of rare earths and non-magnetic materials. *Rep. Prog. Phys.* **42**, 1373 (1979).
 - ² Coey, J. M. D. *Magnetism and Magnetic Materials* (Cambridge Univ. Press, 2010).
 - ³ Hirschberger, M. *Quasiparticle Excitations with Berry Curvature in Insulating Magnets and Weyl Semimetals* (Princeton Univ., 2017).
 - ⁴ Suzuki, T. *et al.* Large anomalous Hall effect in a half-Heusler antiferromagnet. *Nat. Phys.* **12**, 1119–1123 (2016).
 - ⁵ Müller, R. A. *et al.* Magnetic structure of GdBiPt: A candidate antiferromagnetic topological insulator. *Phys. Rev. B* **90**, 041109(R) (2014).
 - ⁶ Canfield, P. C. *et al.* Magnetism and heavy fermion-like behavior in the RBiPt series. *J. Appl. Phys.* **70**, 5800–5802 (1991).
 - ⁷ Ramirez, A. P. Strongly geometrically frustrated magnets. *Annu. Rev. Mater. Sci.* **24**, 453–80 (1994).
 - ⁸ Kresse, G. & Hafner, J. Ab initio molecular dynamics for open-shell transition metals. *Phys. Rev. B* **48**, 13115–13118 (1993).
 - ⁹ Kresse, G. & Furthmüller, J. Efficiency of ab-initio total energy calculations for metals and semiconductors using a plane-wave basis set. *Comp. Mat. Sci.* **6**, 15–50 (1996).
 - ¹⁰ Perdew, J. P., Burke, K. & Ernzerhof, M. Generalized Gradient Approximation Made Simple. *Phys. Rev. Lett.* **77**, 3865–3868 (1996).
 - ¹¹ Mostofi, A. A. *et al.* wannier90: A tool for obtaining maximally-localised Wannier functions. *Comp. Phys. Comm.* **178**, 685–699 (2008).
 - ¹² Shekhar, C. *et al.* Anomalous Hall effect in Weyl semimetal half-Heusler compounds RPtBi (R = Gd and Nd). *Proc. Natl Acad. Sci. USA* (2018).
 - ¹³ Berger, St. *et al.* Crystal structure and thermoelectric properties of novel skutterudites $\text{EpyNi}_4\text{Sb}_{12-x}\text{Sn}_x$ with Ep = Sn, Eu and Yb. *Proc. 21st International Conference on Thermoelectrics IEEE*, 48 (2002).
 - ¹⁴ Honig, J. & Harman, T. Galvano-thermomagnetic effects in multi-band models. *Adv. Energy Conv.* **3**, 529–536 (1963).
 - ¹⁵ Shoenberg, D. *Magnetic Oscillations in Metals* (Cambridge Univ. Press, 1984).
 - ¹⁶ Hirschberger, M. *et al.* The chiral anomaly and thermopower of Weyl fermions in the half-Heusler GdPtBi. *Nat. Mater.* **15**, 1161–1165 (2016).
 - ¹⁷ Lakeshore Ruthenium Oxide (Rox) RTDs. URL https://www.lakeshore.com/Documents/LSTC_Rox_1.pdf (2018).
 - ¹⁸ Affronte, M., Campani, M., Morten, B., Prudenziati, M. & Laborde, O. Magnetoresistance of RuO₂-Based Thick Film Resistors. *J. Low Temp. Phys.* **112**, 355–371 (1998).
 - ¹⁹ Lakeshore Cernox RTDs. URL https://www.lakeshore.com/Documents/LSTC_Cernox_1.pdf (2018).
 - ²⁰ Brandt, B. L., Liu, D. W. & Rubin, L. G. Low temperature thermometry in high magnetic fields. VII. CernoxTM sensors to 32 T. *Rev. Sci. Instr.* **70**, 104–110 (1999).
 - ²¹ Landsteiner, K., Megías, E. & Pena-Benitez, F. Gravitational Anomaly and Transport Phenomena. *Phys. Rev. Lett.* **107**, 021601 (2011).
 - ²² Stone, M. & Kim, J. Mixed anomalies: Chiral vortical effect and the Sommerfeld expansion. *Phys. Rev. D* **98**, 025012 (2018).
 - ²³ Loganayagam, R. & Surówka, P. Anomaly/transport in an Ideal Weyl gas. *J. High Energy Phys.* **4**, 97 (2012).
 - ²⁴ Jensen, K., Loganayagam, R. & Yarom, A. Thermodynamics, gravitational anomalies and cones. *J. High Energy Phys.* **2**, 88 (2013).
 - ²⁵ Golkar, S. & Sethi, S. Global anomalies and effective field theory. *J. High Energy Phys.* **5**, 105 (2016).
 - ²⁶ Chowdhury, S. D. & David, J. R. Global gravitational anomalies and transport. *J. High Energy Phys.* **12**, 116 (2016).
 - ²⁷ Lucas, A., Davison, R. A. & Sachdev, S. Hydrodynamic theory of thermoelectric transport and negative magnetoresistance in Weyl semimetals. *Proc. Natl. Acad. Sci. USA* **113**, 9463–9468 (2016).
 - ²⁸ Landsteiner, K., Megías, E., Melgar, L. & Pena-Benitez, F. Holographic gravitational anomaly and chiral vortical effect. *J. High Energy Phys.* **9**, 121 (2011).
 - ²⁹ Son, D. T. & Surówka, P. Hydrodynamics with Triangle Anomalies. *Phys. Rev. Lett.* **103**, 191601 (2009).
 - ³⁰ Gooth, J. *et al.* Experimental signatures of the mixed axial-gravitational anomaly in the Weyl semimetal NbP. *Nature* **547**, 324–327 (2017).
 - ³¹ Landsteiner, K. & Liu, Y. Anomalous transport model with axial magnetic fields. *Phys. Lett. B* **783**, 446–451 (2018).
 - ³² Landsteiner, K., Megías, E. & Pena-Benitez, F. Anomalous Transport from Kubo Formulae. In: *Strongly Interacting Matter in Magnetic Fields. Lecture Notes in Physics, vol. 871* (Springer, Berlin, Heidelberg, 2013).
 - ³³ LeBellac, M. *Thermal Field Theory* (Cambridge Univ. Press, 2000).